Ultrasmall copper-based nanoparticles for reactive oxygen species scavenging and alleviation of inflammation related diseases

Liu *et al.*

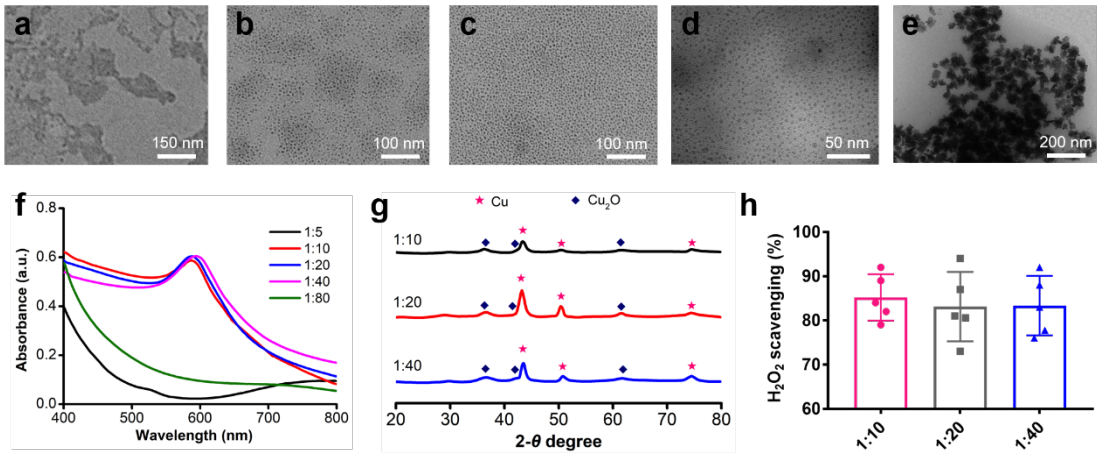

Supplementary Figure 1. Optimization of the ratio of Cu^{2+} to L-ascorbic acid (AA). TEM images of the synthesized copper based nanoparticles with various concentrations of L-ascorbic acid. (**a**) 1:5; (**b**) 1:10; (**c**) 1:20; (**d**) 1:40; (**e**) 1:80; (**f**) The UV-Vis absorption spectra of copper based nanoparticles stabilized in L-ascorbic acid aqueous solution with various concentrations; (**g**) XRD patterns of deposits after in the reactions of different concentration of L-ascorbic acid; (**h**) H_2O_2 scavenging of copper based nanoparticles obtained by different concentration of AA. In **h**, data represent means ± s.d. from five independent replicates. Source data are provided as a Source Data file.

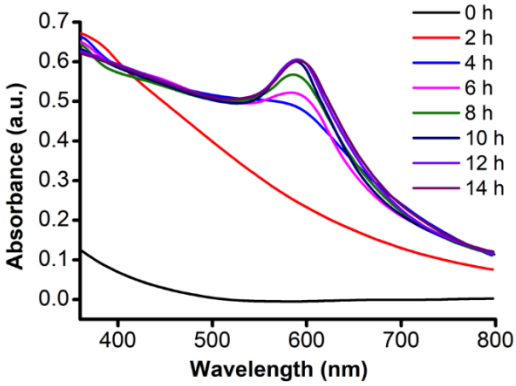

Supplementary Figure 2. Optimization of the reaction time. The UV-Vis absorption spectra of copper based nanoparticles at different time point. Source data are provided as a Source Data file.

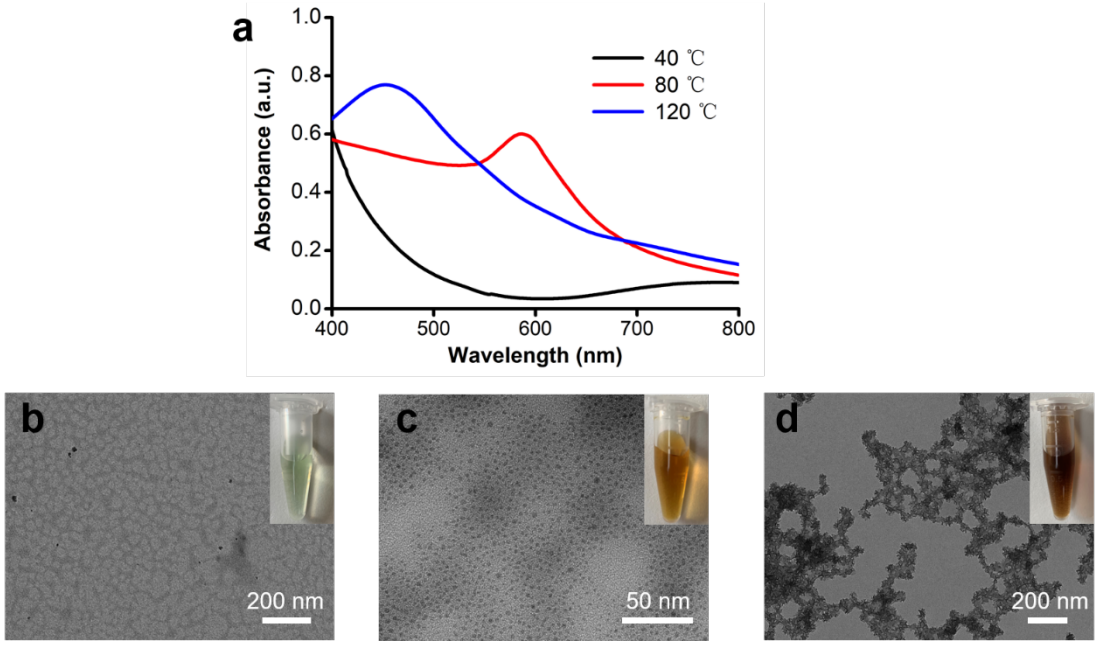

Supplementary Figure 3. Optimization of the reaction temperature. (**a**) The UV-Vis absorption spectra of copper based nanoparticles obtained in different temperatures; TEM images of the synthesized copper based nanoparticles at different temperatures. (**b**) 40 ℃; (**c**) 80 ℃; (**d**) 120 ℃. Inserted photographs are the obtained dispersions, repectively. Source data are provided as a Source Data file.

Optimization of the reaction condition of copper-based nanoparticles

Generally, the molar ratio of reactants, reaction temperature and reaction time can influence the final products. Therefore, we optimized reaction conditions to tune the physiochemical properties of the nanoparticles, as well as their catalytic activity. Firstly, the impact of feeding molar ratio between Cu^{2+} and AA was studied. Briefly, 10 mM $CuCl_2$ powders were added in the water (50 mL), and stirred for 10 min at 80 ^oC until completely dissolve. Then, 50 mL AA aqueous solution with a series of concentrations (50 mM, 100 mM, 200 mM, 400 mM and 800 mM), were added slowly to the above $CuCl_2$ solution, respectively. The mixture was kept at 80 ^oC for 14-16 h with constantly stirring. Then, the copper based nanoparticles were dialyzed for 2 days, and concentrated with centrifugation.

It is observed that the initial molar ratio of Cu^{2+}: AA can affect the formation of copper based nanoparticles. The TEM images (Supplementary Figure 1b-d) showed that all the nanoparticles were about 3~4 nm in diameter, within a certain range of the Cu^{2+}: AA ratio (from 1:10 to 1:40). The XRD patterns of these copper based nanoparticles determined by changing the molar ratio of reactants from 1:10 to 1:40 indicated that the Cu (0) and Cu_2O (I) coexisted in these nanoparticles (Supplementary Figure 1g). The absorbance peak of these nanoparticles was appeared around 580 nm (Supplementary Figure 1f). With the molar ratio of Cu^{2+}: AA increasing, the absorbance peak of these copper based nanoparticles showed a slight red-shift within 5 nm, which was possibly due to the slight size change.[1,2] However, there was no obvious nanoparticle formed (Supplementary Figure 1a) and absorbance

peak appeared with the molar ratio of Cu^{2+}: AA equal to 1:5 (Supplementary Figure 1f). Upon the molar ratio of Cu^{2+}: AA increased to 1:80, a large number of brass colored precipitate obtained within 10 min after the AA added and there is no absorbance peak appeared as expected (Supplementary Figure 1f).

Among biologically relevant ROS (O_2•$^-$, H_2O_2 and •OH), H_2O_2 is of greatest importance because of its membrane permeability, longer half-life than O_2•$^-$ and •OH, and consequently highest intracellular concentration.[3] Hence, the comparative H_2O_2 scavenging capacity of the obtained copper nanoparticles by changing the molar ratio of Cu^{2+}: AA from 1:10 to 1:40 was further studied. As shown in Supplementary Figure 1h, with the molar ratio of Cu^{2+}: AA increasing, the H_2O_2 scavenging capacity of copper based nanoparticles showed a slight reduction, but without significant difference ($p > 0.05$). In conclusion, the molar ratio of Cu^{2+}: AA equal to 1:10 was chosen for the following study.

Additionally, the reaction time was considered. The samples at determined time points (0 h, 2 h, 4 h, 6 h, 8 h, 10 h, 12 h and 14 h) during the reaction were collected and their absorbance peaks were measured (Supplementary Figure 2). Initially, there is no characteristic absorption peak appeared within the first 4 h reaction. With the reaction time further increasing, the characteristic absorption peak (~580 nm) appeared and the peak intensity also increased, which are possibly due to the growth of copper based nanoparticles. However, until the reaction time up to 10 h, the UV-Vis-NIR spectra were almost overlapped with the further increasing the reaction time,

indicating that the reaction was completed after reaction 10 h. Therefore, to obtain stable copper based nanoparticles, the agitation time should be extended to 10 h.

As the temperature as an important parameter for controlling the formation of copper based nanoparticles, the temperatures of 40 ºC, 80 ºC and 120 ºC were chosen to study the temperature effects. Under the 40 ºC reaction, there were no characteristic peak appeared (Supplementary Figure 3a), which was further verified by the no obvious nanoparticles formed (Supplementary Figure 3b). While the temperature climbed to 120 ºC, a new characteristic absorption peak appeared at ~470 nm (Supplementary Figure 3a) and a lot aggregated nanoparticles formed (Supplementary Figure 3d). These phenomena was largely due to the lower temperature (40 ºC) failed to induce the reduction reaction, while the higher temperature (120 ºC) may cause the dissolved oxygen reduction and also make AA molecules degrade rapidly.

In Summary, the molar ratio of Cu^{2+}: AA equals to 1:10, 80 ºC reaction temperature and 12 h reaction time were the optimum conditions for this reaction.

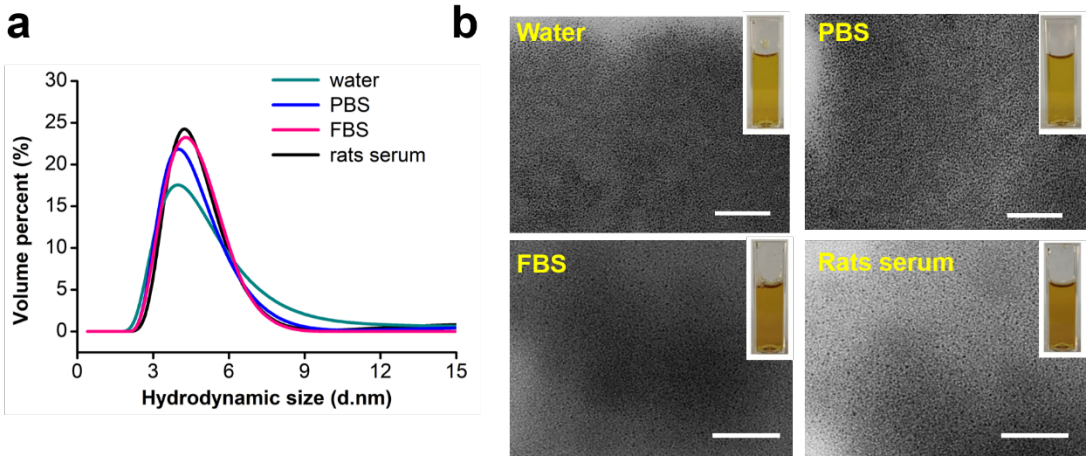

Supplementary Figure 4. The stability of $Cu_{5.4}O$ USNPs in different media. (**a**) Hydrodynamic diameter distribution of the $Cu_{5.4}O$ USNPs in water, PBS, FBS and rats serum after 20 days. (**b**) TEM images of $Cu_{5.4}O$ USNPs in water, PBS, FBS and rats serum after 20 days, respectively. Scale bars are 50 nm. Inserts are the photographs of $Cu_{5.4}O$ USNPs dispersed in the different media for 20 days, respectively. Source data are provided as a Source Data file.

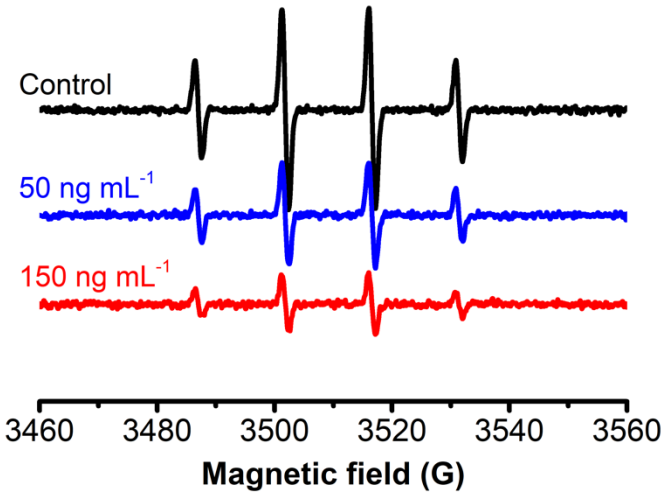

Supplementary Figure 5. ·OH scavenging of $Cu_{5.4}O$ USNPs determined by EPR. The sample solution contained 100 mM DMPO, 2 mM H_2O_2, 10 μM $FeSO_4$ and

variable concentration of $Cu_{5.4}O$ USNPs (0, 50, 150 ng·mL^{-1}) in HAc/NaAc buffer (0.5 M, pH 4.5). Source data are provided as a Source Data file.

Supplementary Table 1. Summary of ROS scavenging nanomaterials.

Materials	In vitro antioxidative activities	In vivo antioxidative activities
Melanin-based Nanoparticles[4]	79.4 ± 4.7% of $O_2\cdot^-$ at 25 μg·mL^{-1}; 68.4 ± 2.5% of ·OH at 100 μg·mL^{-1}; 85.2 ± 2.3% of ABTS at 100 μg·mL^{-1};	25 mg·kg^{-1} for AKI
DNA origami nanostructures[5]	50% of $O_2\cdot^-$ at 1.65 μg·mL^{-1}; 30% of ·OH at 1.65 μg·mL^{-1}; 50% of ABTS at 1.65 μg·mL^{-1};	0.5 mg·kg^{-1} for AKI
Molybdenum-based nanoclusters[6]	50% of $O_2\cdot^-$ at 80 μg·mL^{-1}; 60% of ·OH at 20 μg·mL^{-1}; 95% of ABTS at 20 μg·mL^{-1};	50 mg·kg^{-1} for AKI
Cu-TCPP nanosheets[7]	90% of $O_2\cdot^-$ at 5.5 μg·mL^{-1};	0.8 mg·kg^{-1} for AKI
Ceria nanoparticles[8]	90% of H_2O_2 at 0.6 mM (84 μg·mL^{-1}); 40% of $O_2\cdot^-$ at 0.6 mM (84 μg·mL^{-1}); 50% of ·OH at 0.6 mM (84 μg·mL^{-1});	0.6 mg·kg^{-1} for hepatic ischemia-reperfusion injury
TPCD nanoparticles[9]	Not given	1 mg kg^{-1} for AILI
MSN-Ceria nanocomposites[10]	83% of H_2O_2 at 1.5 mM (210 μg mL^{-1}); 55% of $O_2\cdot^-$ at 0.12 mM (14 μg·mL^{-1});	2.5-3.3 mg kg^{-1} for wound healing
Ultrasmall $Cu_{5.4}O$ nanoparticles	80% of H_2O_2 at 200 ng·mL^{-1}; 50% of $O_2\cdot^-$ at 150 ng·mL^{-1}; 80% of ·OH at 150 ng·mL^{-1}; 89% of ABTS at 150 ng·mL^{-1};	2 μg·kg^{-1} for AKI; 6 μg·kg^{-1} for AILI; 320-400 ng·kg^{-1} for wound healing

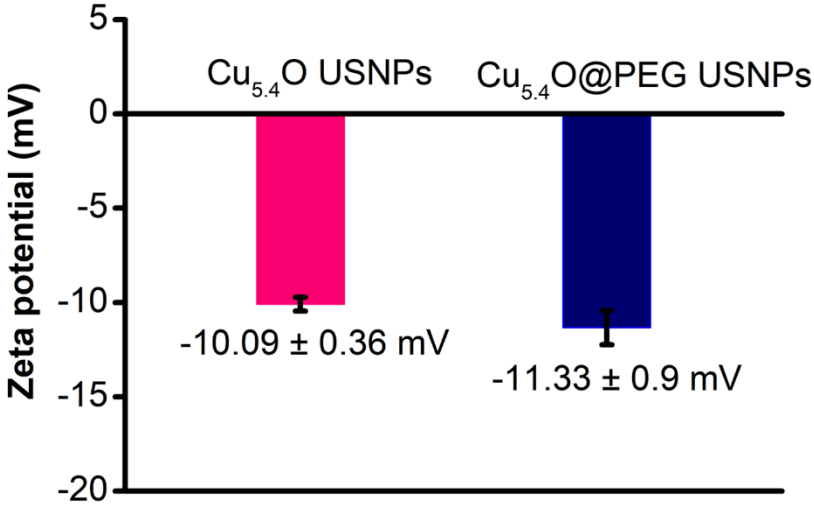

Supplementary Figure 6. Zeta potential of $Cu_{5.4}O$ and $Cu_{5.4}O$@PEG USNPs. Source data are provided as a Source Data file.

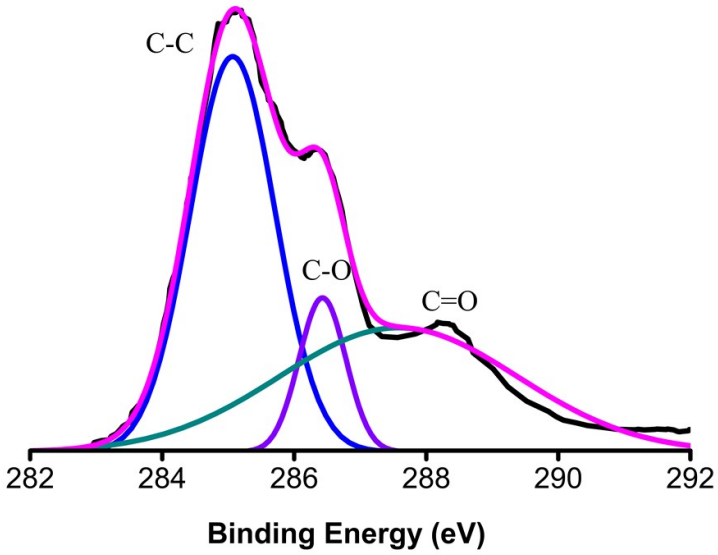

Supplementary Figure 7. The C1s XPS spectra of the $Cu_{5.4}O$ USNPs. Source data are provided as a Source Data file.

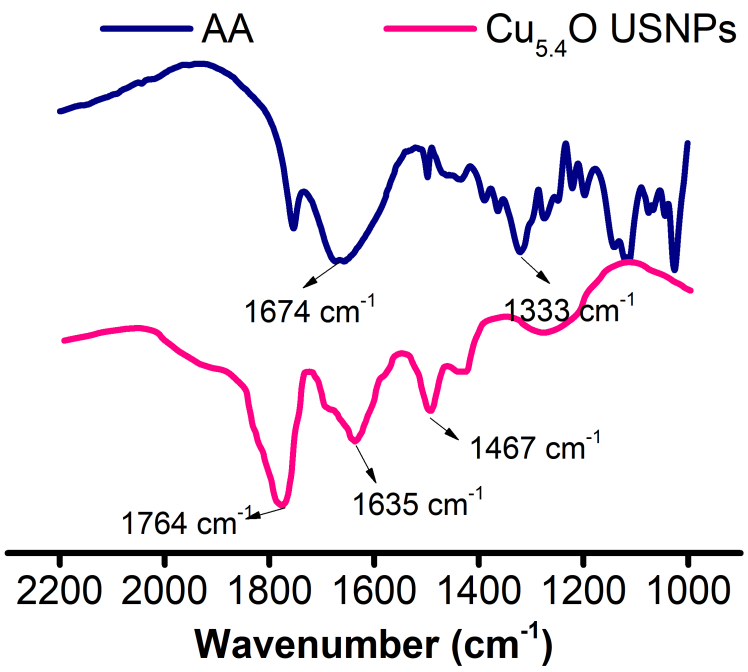

Supplementary Figure 8. FTIR spectra of AA and $Cu_{5.4}O$ USNPs. Source data are provided as a Source Data file.

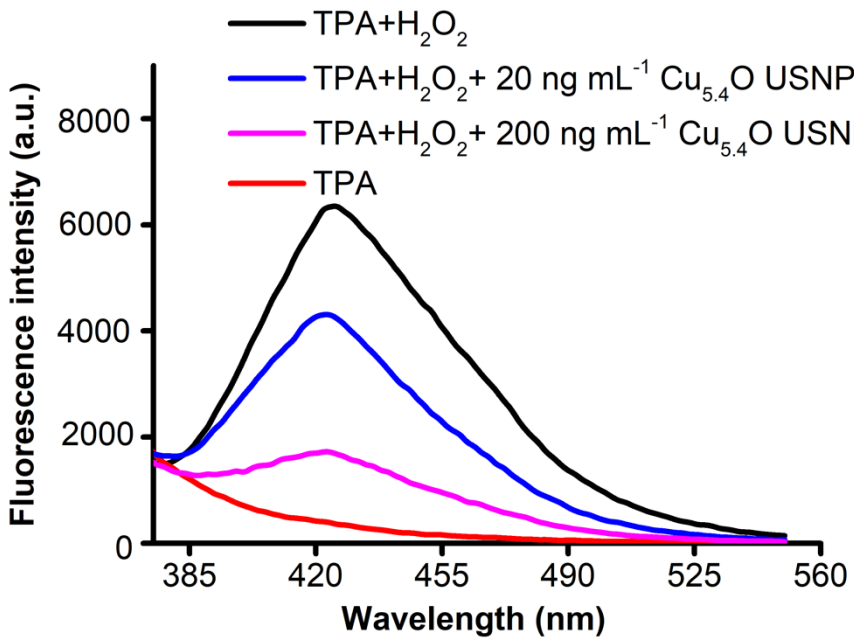

Supplementary Figure 9. H_2O_2 scavenging property of $Cu_{5.4}O$ USNPs. Fluorescence spectra of TPA, TPA + H_2O_2, TPA + H_2O_2 + $Cu_{5.4}O$ USNPs (20 or 200 ng mL^{-1}), respectively. Source data are provided as a Source Data file.

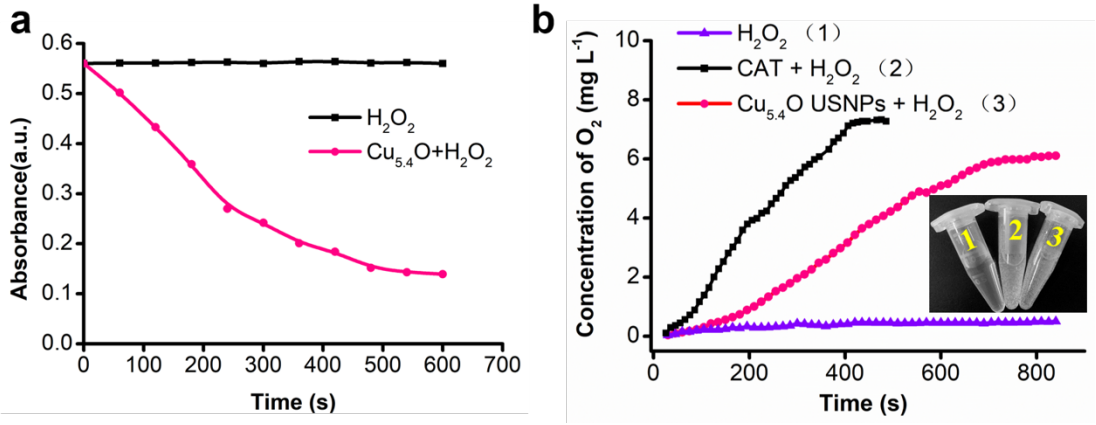

Supplementary Figure 10. The CAT-like activity of the $Cu_{5.4}O$ USNPs. (**a**) Plot of the absorbance versus time for the reaction of H_2O_2 (2mM) in the presence of $Cu_{5.4}O$ USNPs (250 ng mL^{-1}). (**b**) O_2 generation from H_2O_2 catalyzed by $Cu_{5.4}O$ USNPs or CAT was recorded. Inset photo is the formation of bubbles, revealing the decomposition of H_2O_2 by the $Cu_{5.4}O$ USNPs or CAT. Source data are provided as a Source Data file.

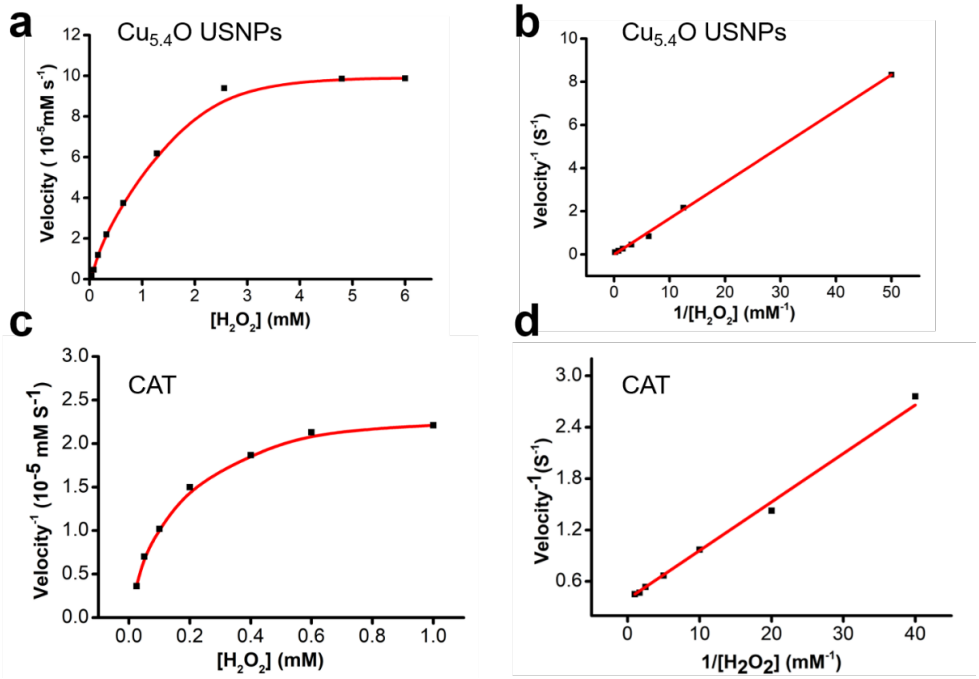

Supplementary Figure 11. Steady-state kinetics of $Cu_{5.4}O$ USNPs. Steady-state constant of the (**a**) CAT and the (**b**) CAT-like activity of $Cu_{5.4}O$ USNPs in PBS (10 mM, pH 7.4) at 25 ºC with H_2O_2 as substrate.[11] The corresponding double reciprocal plots of (**c**) CAT and (**d**) $Cu_{5.4}O$ USNPs. Source data are provided as a Source Data file.

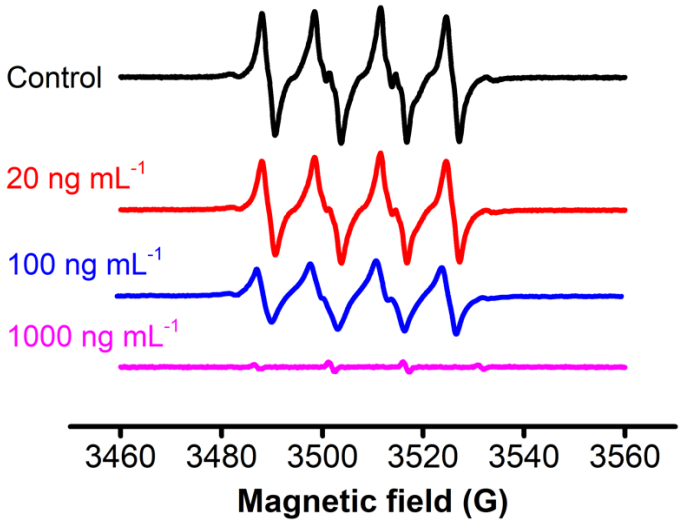

Supplementary Figure 12. The SOD-like activity of the $Cu_{5.4}O$ USNPs. EPR spectra were recorded from samples containing 10 mM PBS, 5 mM xanthine, and 0.5 U mL^{-1}

xanthine oxidase, containing $Cu_{5.4}O$ USNPs (20, 100 and 1000 ng mL^{-1}) or not (Control). Source data are provided as a Source Data file.

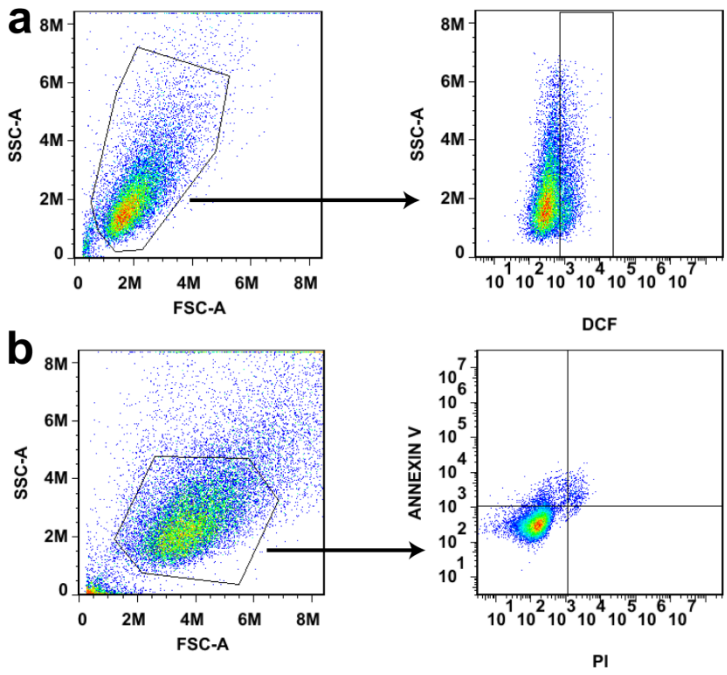

Supplementary Figure 13. Gating strategies of flow cytometry. (**a**) Gating strategy to determine the intracellular ROS level presented in Fig. 4b. (**b**) Gating strategy to determine the percentage of Annexin V-FITC$^+$ PI$^+$ and Annexin V-FITC$^+$ PI$^-$ cells presented in Fig. 4e.

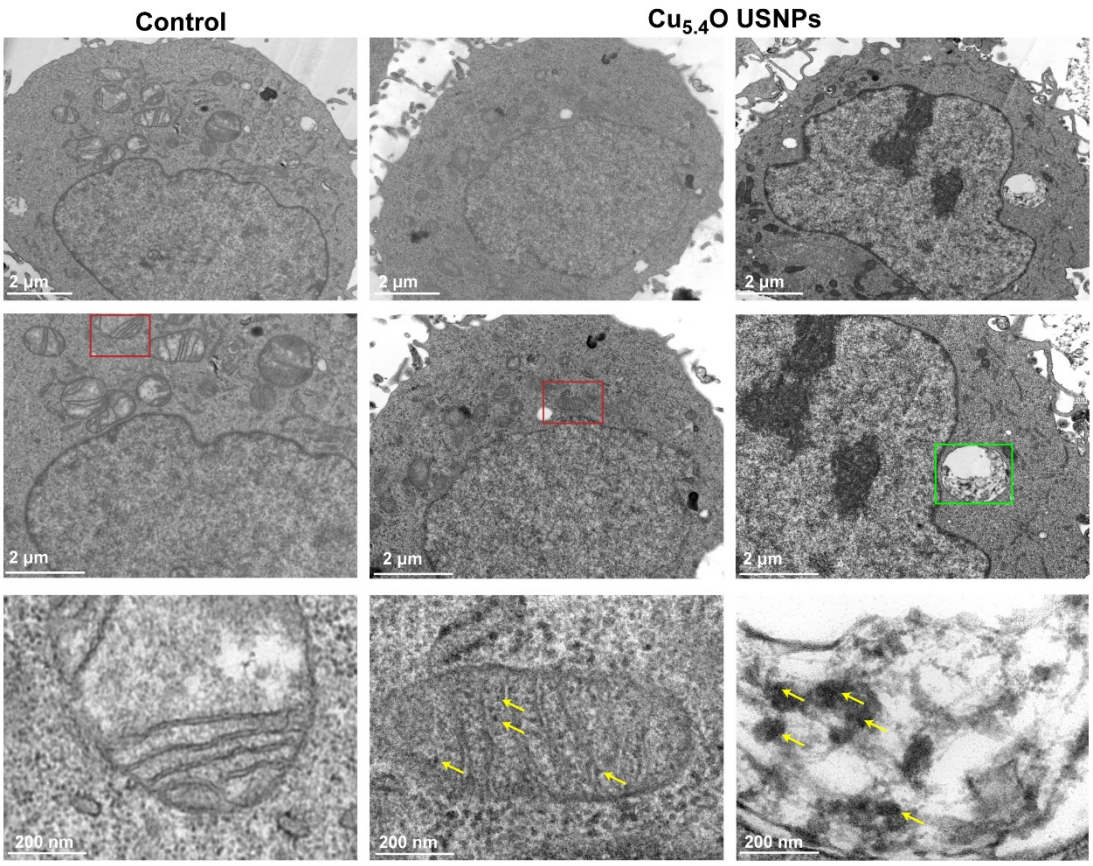

Supplementary Figure 14. TEM images of $Cu_{5.4}O$ USNPs in cells. The untreated cells were considered as control. The $Cu_{5.4}O$ USNPs (yellow arrow headed) were located in the mitochondria (red square) and phagosome (green square).

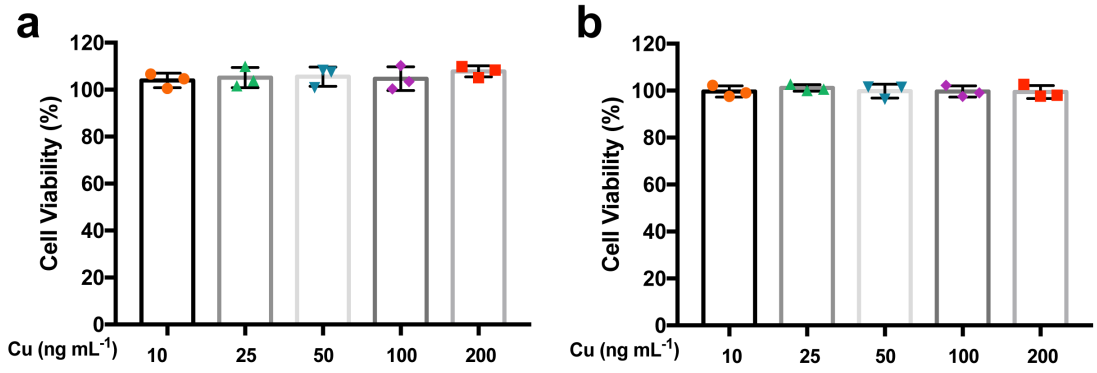

Supplementary Figure 15. In vitro cytotoxicity of $Cu_{5.4}O$ USNPs. In vitro cytotoxicity of $Cu_{5.4}O$ USNPs towards HEK 293 cells after incubation for (**a**) 24 and

(**b**) 48 h. Data represent means ± s.d. from three independent replicates. Source data are provided as a Source Data file.

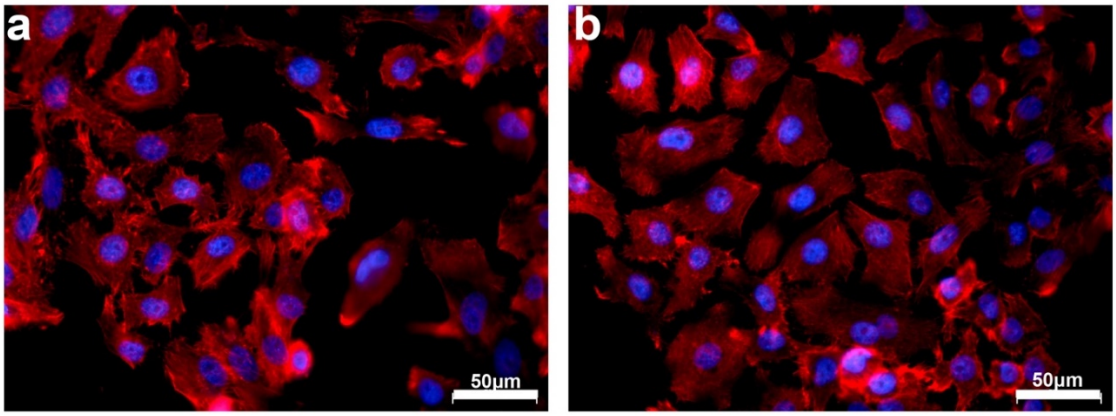

Supplementary Figure 16. Cytoskeleton staining of HEK 293 cells. (**a**) Cytoskeleton staining of HEK 293 cells in control group. (**b**) Cytoskeleton staining of HEK 293 cells after incubation with $Cu_{5.4}O$ USNPs at 200 ng mL^{-1} concentration for 48h. Red and blue fluorescence indicate cytoskeleton and nucleus, respectively.

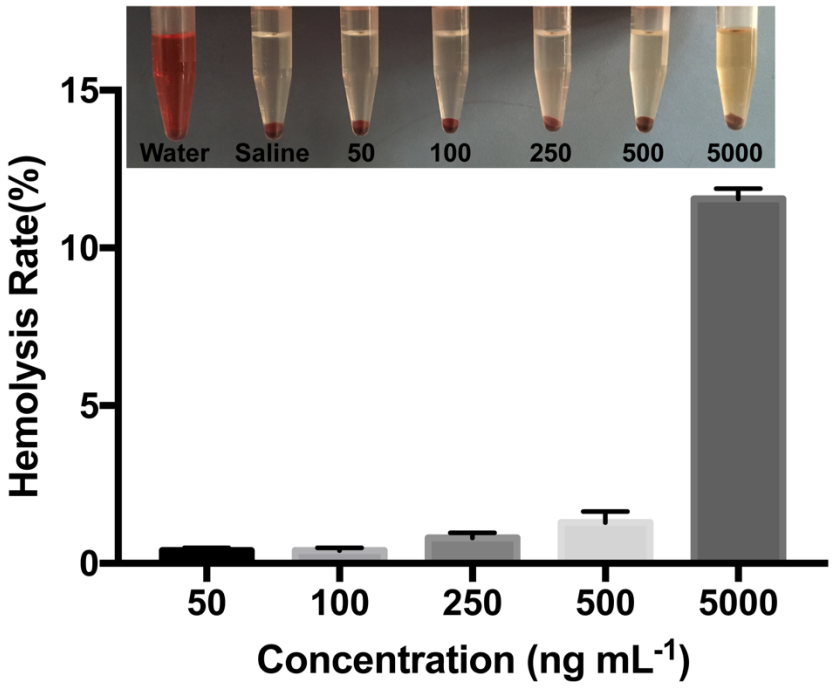

Supplementary Figure 17. In vitro hemolysis test of $Cu_{5.4}O$ USNPs. Data represent means ± s.d. from three independent replicates. Source data are provided as a Source Data file.

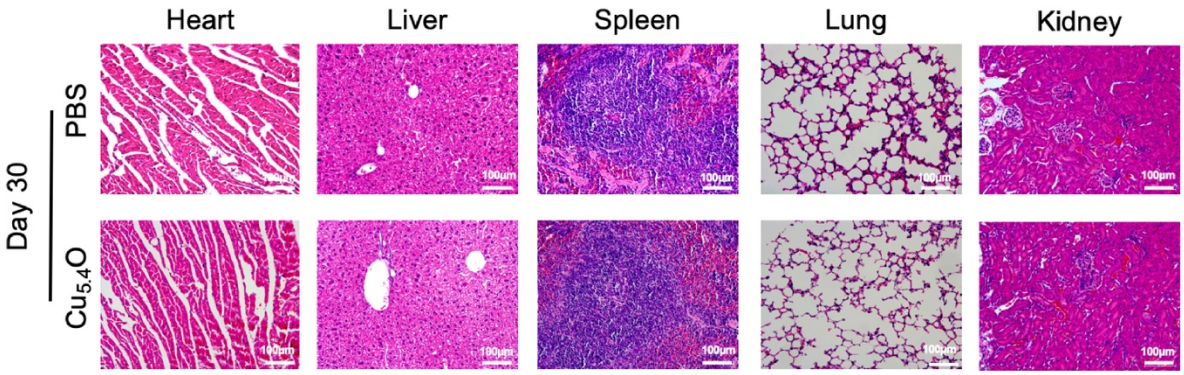

Supplementary Figure 18. In vivo toxicity of $Cu_{5.4}O$ USNPs. In vivo toxicity evaluation of $Cu_{5.4}O$ USNPs to major organs (heart, liver, spleen, lung, and kidney) 30 days after intravenous administration.

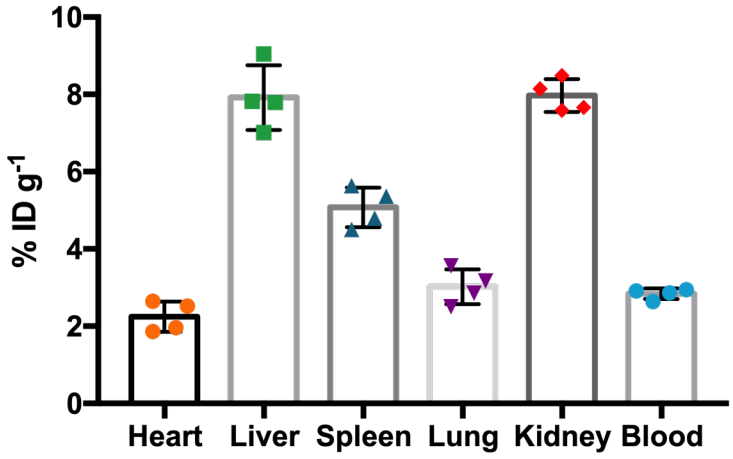

Supplementary Figure 19. Biodistribution of $Cu_{5.4}O$ USNPs. Biodistribution of $Cu_{5.4}O$ USNPs in the major organs after repeated administration for seven consecutive days. Data represent means ± s.d. from four independent replicates. Source data are provided as a Source Data file.

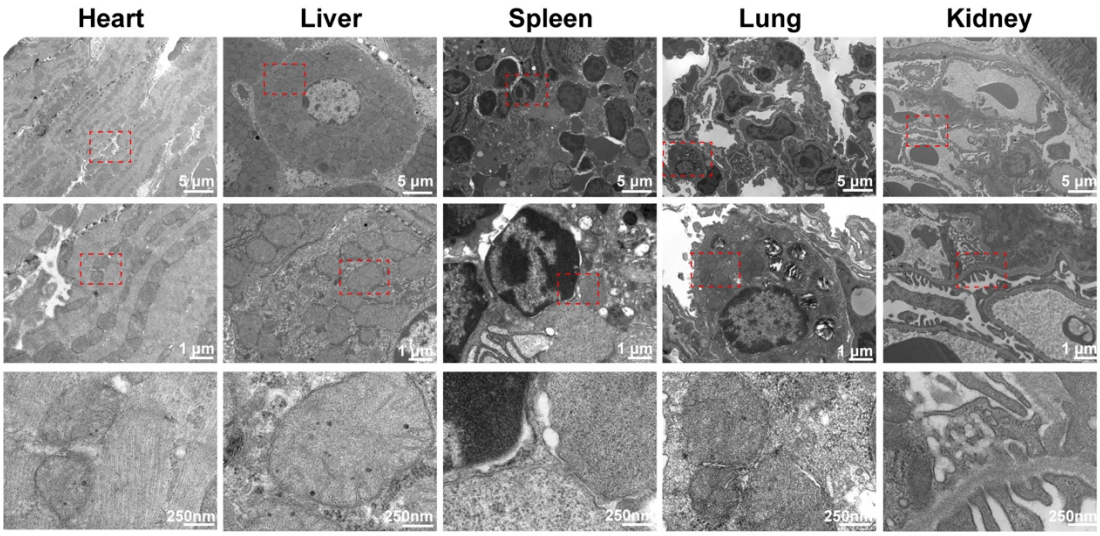

Supplementary Figure 20. Accumulation of $Cu_{5.4}O$ USNPs in major organs. Accumulation of $Cu_{5.4}O$ USNPs in the major organs after repeated administration for seven consecutive days by TEM observation. Red dashed lines indicate the magnified area.

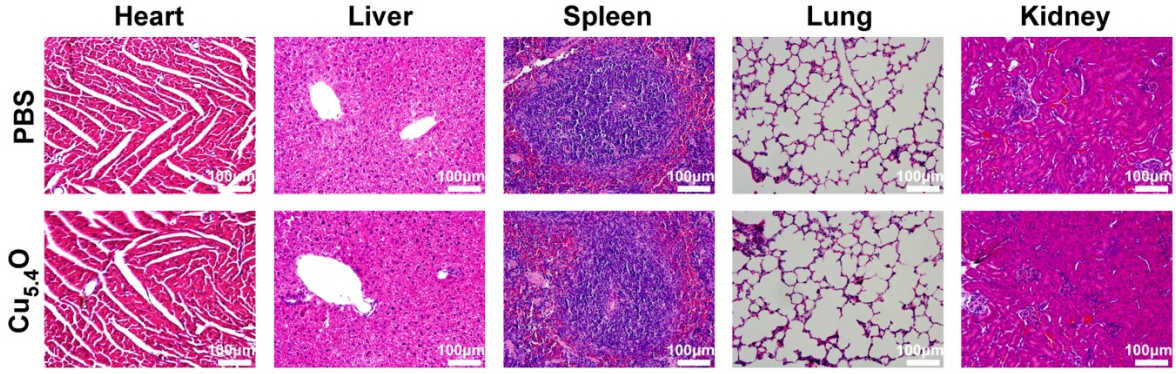

Supplementary Figure 21. In vivo toxicity of $Cu_{5.4}O$ USNPs. In vivo toxicity evaluation of $Cu_{5.4}O$ USNPs to major organs (heart, liver, spleen, lung, and kidney) after repeated intravenous administration for seven consecutive days.

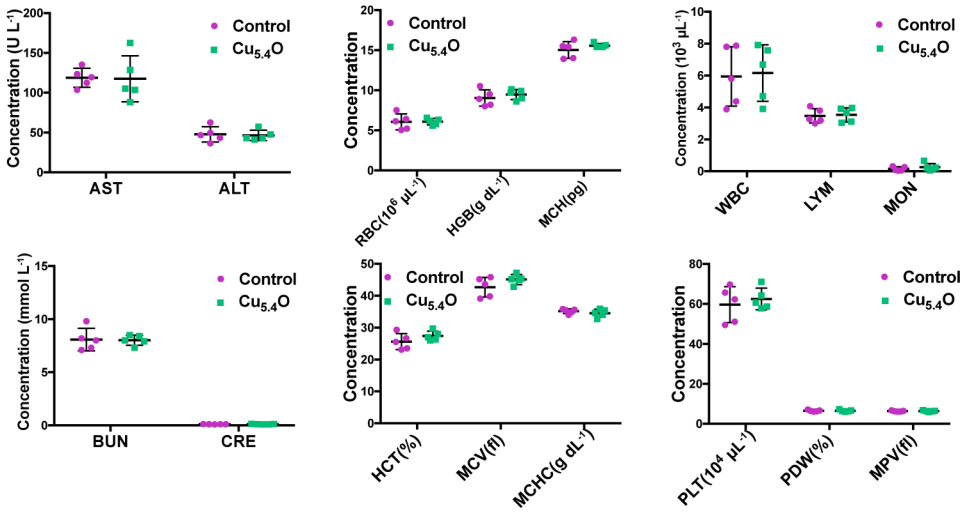

Supplementary Figure 22. In vivo biosafety of $Cu_{5.4}O$ USNPs. Serum biochemistry analysis and complete blood panel analysis results of mice after repeated administration of $Cu_{5.4}O$ USNPs for seven consecutive days. Data represent means ± s.d. from five independent replicates. Source data are provided as a Source Data file.

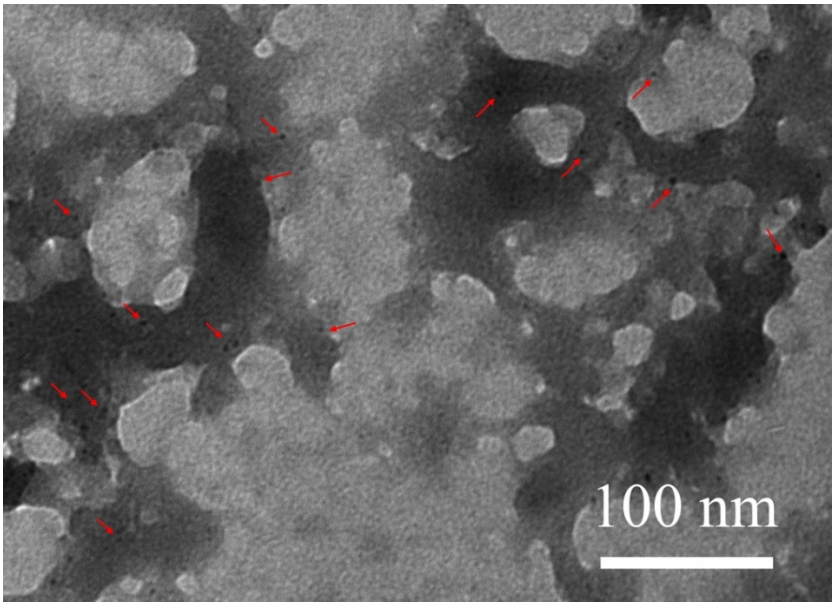

Supplementary Figure 23. $Cu_{5.4}O$ USNPs in the urine.TEM image of the urine from the mouse after injection with $Cu_{5.4}O$ USNPs. Red arrows indicated $Cu_{5.4}O$ USNPs.

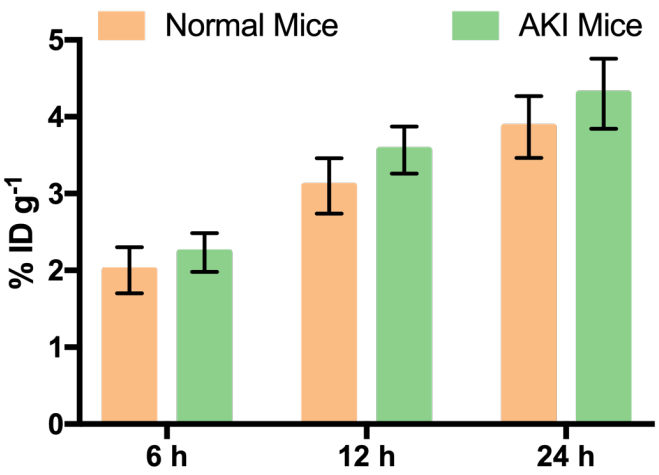

Supplementary Figure 24. Accumulation of $Cu_{5.4}O$ USNPs in the kidney. Time-dependent accumulation of $Cu_{5.4}O$ USNPs in the kidney of normal and AKI mice. Data represent means ± s.d. from three independent replicates. Source data are provided as a Source Data file.

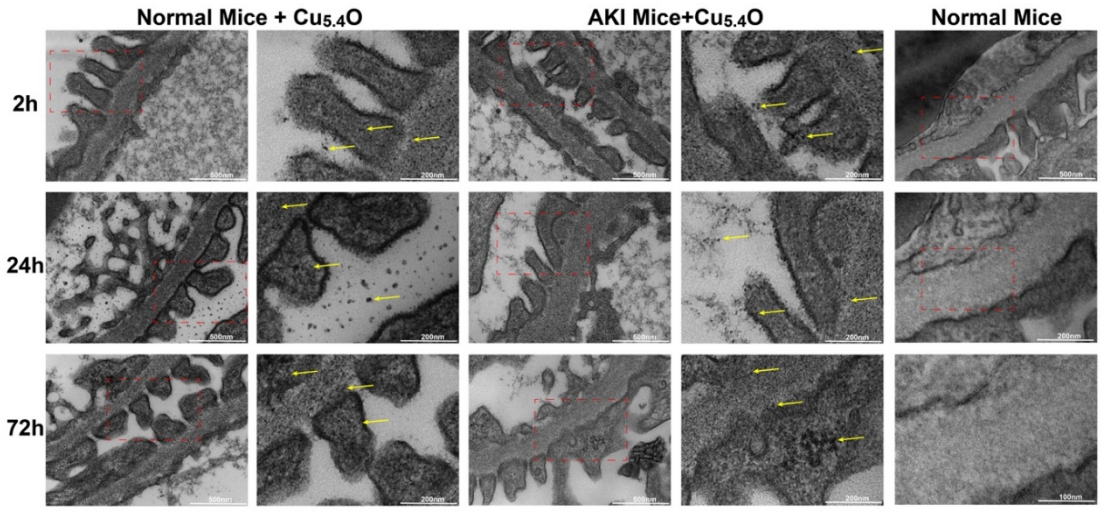

Supplementary Figure 25. Biodistribution of $Cu_{5.4}O$ USNPs in renal tissues. Biodistribution of $Cu_{5.4}O$ USNPs in the glomerular basement membrane at different time points by TEM observation. Yellow arrows indicate $Cu_{5.4}O$ USNPs. Red dashed lines indicate magnified area.

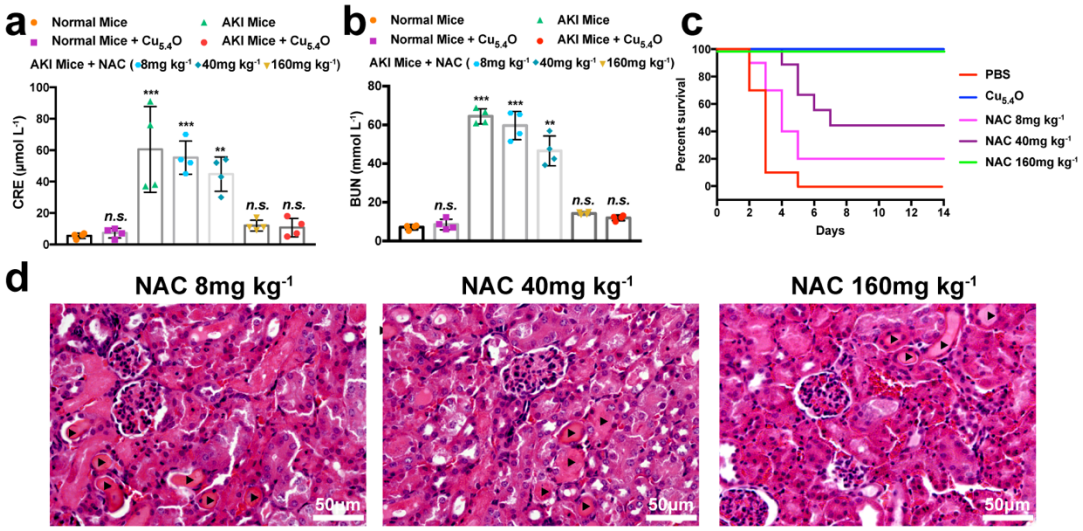

Supplementary Figure 26. Treatment of AKI. Serum levels of (**a**) CRE and (**b**) BUN in AKI mice at 24 h after different treatment. (**c**) Survival curves of AKI mice with different treatment. (**d**) H&E staining of kidney tissues from different NAC treatment group. Triangles indicate the formation of casts. Statistical difference was compared between normal and different treatment groups In **a** and **b**, data represent means ± s.d. from four independent replicates. (**$P < 0.01$; ***$P < 0.001$; n.s., no significance, One-way ANOVA) Source data are provided as a Source Data file.

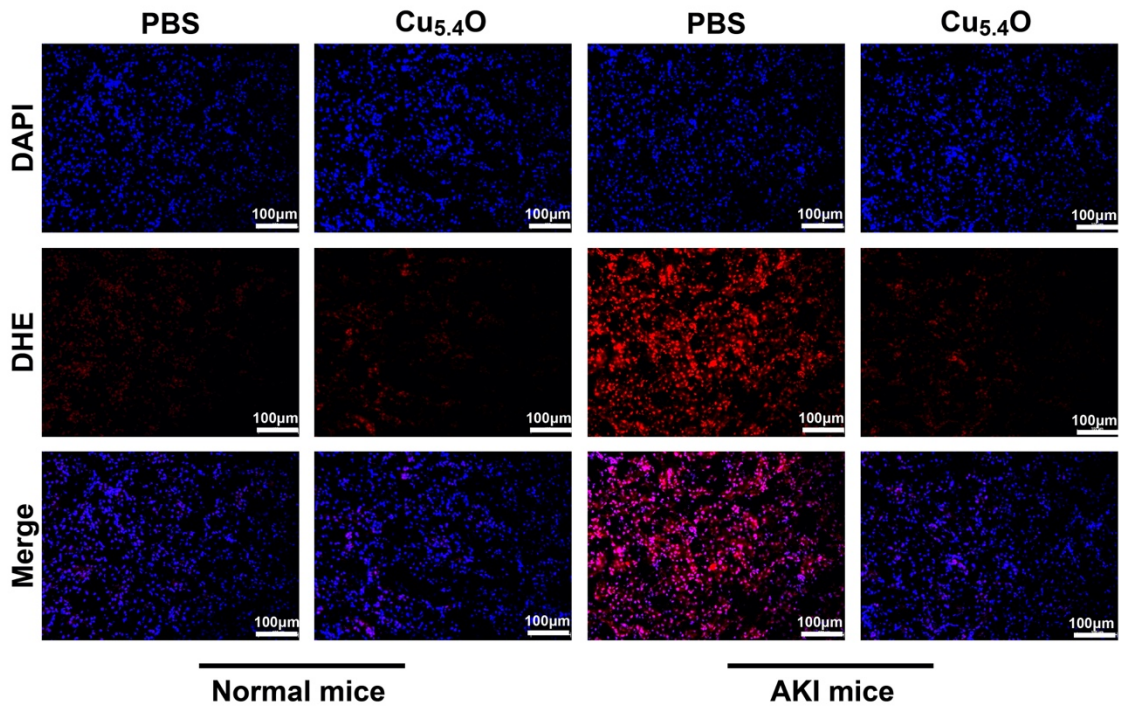

Supplementary Figure 27. DHE and DAPI staining of kidney tissues. Red and blue fluorescence indicate DHE and DAPI respectively.

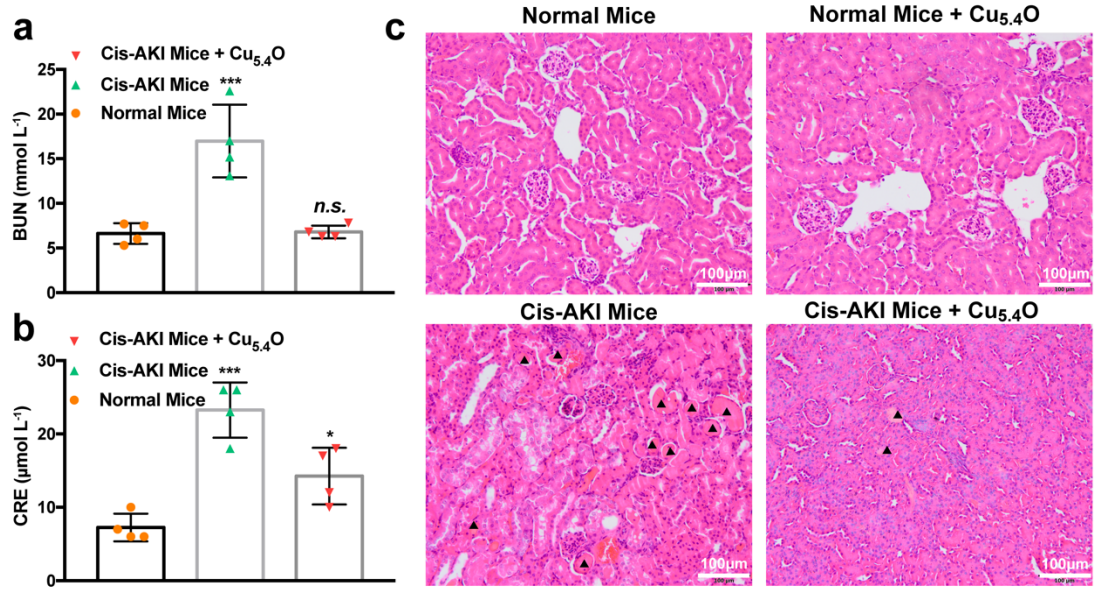

Supplementary Figure 28. Treatment of Cis-AKI. (**a**) BUN and (**b**) CRE levels in the blood serum from each group. (**c**) H&E staining of kidney tissues from each group.

Triangles indicate the formation of casts. In **a** and **b**, data represent means ± s.d. from four independent replicates. (*$P < 0.05$; ***$P < 0.001$; n.s., no significance, One-way ANOVA) Source data are provided as a Source Data file.

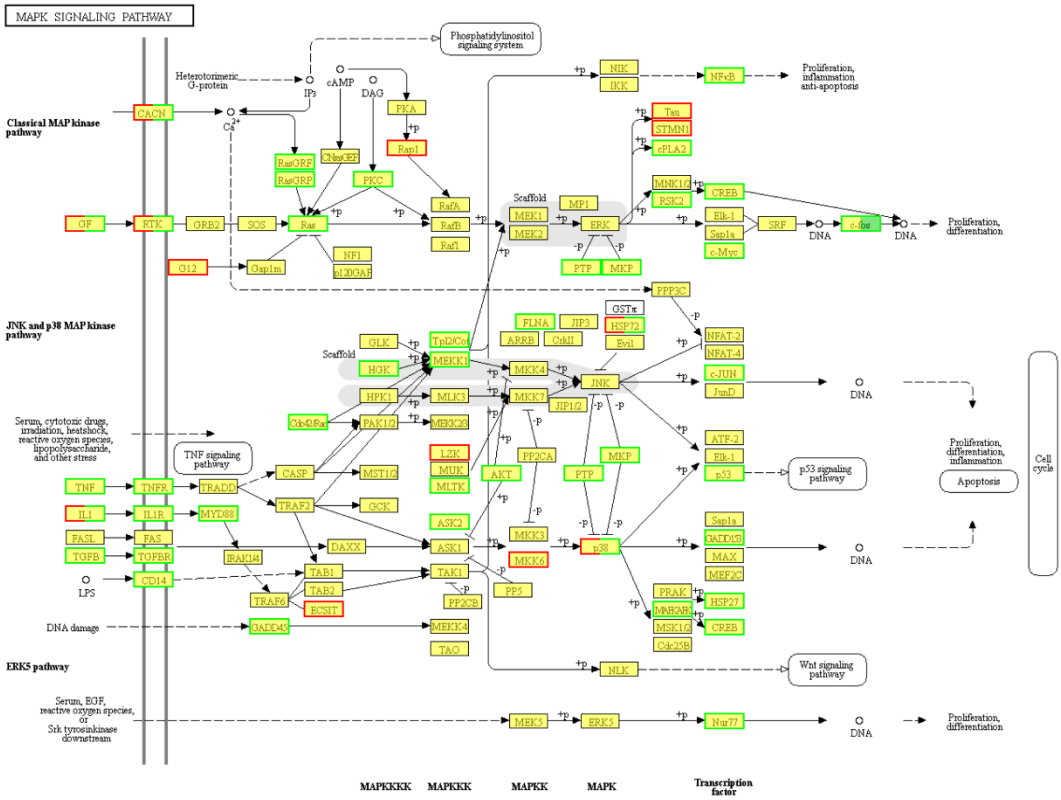

Supplementary Figure 29. KEGG pathway of enriched MAPK signaling pathway. Red and green outlines represent up-regulated DEGs and down-regulated DEGs, respectively.

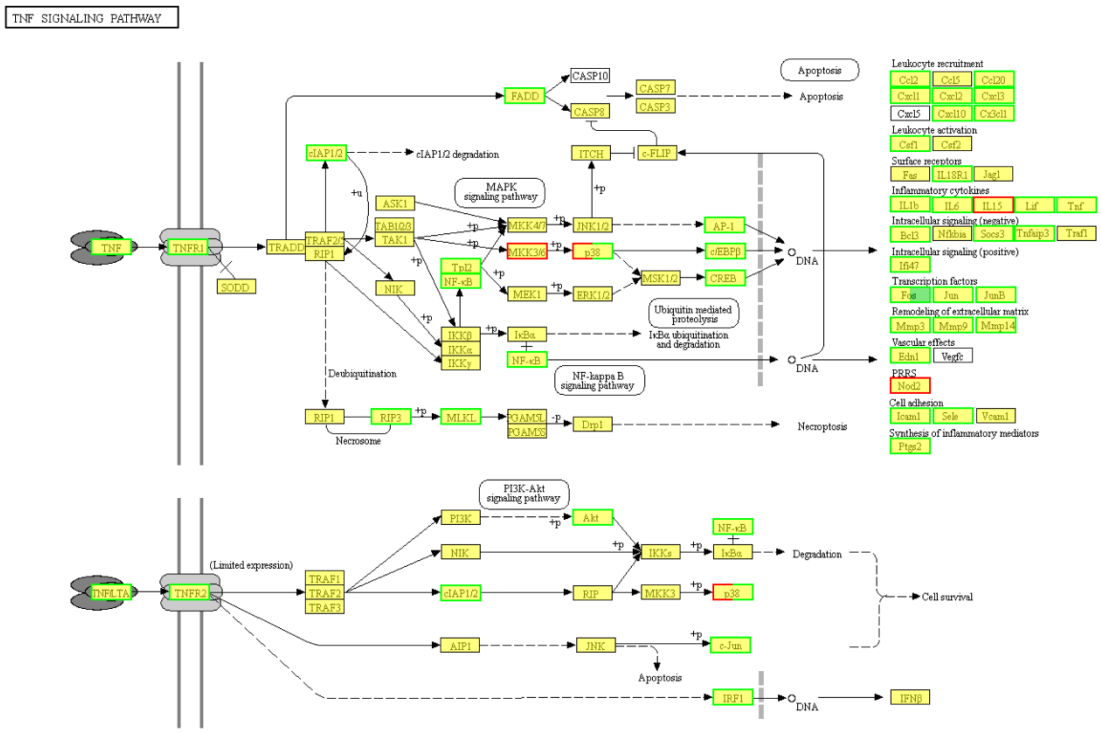

Supplementary Figure 30. KEGG pathway of enriched TNF signaling pathway. Red and green outlines represent up-regulated DEGs and down-regulated DEGs, respectively.

Supplementary Table 2. Sequences of the primers used for qRT-PCR

Gene	Forward sequences	Reverse sequences
Mouse SOD1	5-GCGGTGAACCAGTTGTGTTG-3	5-CCCCATACTGATGGACGTGG-3
Mouse SOD2	5-GTAGGGCCTGTCCGATGATG-3	5-CGCTACTGAGAAAGGTGCCA-3
Mouse SOD3	5-TCCCACAAGCCCCTAGTCTT-3	5-TGAGCACATGCGATCTCTGG-3
Mouse CAT	5-ACAAGATTGCCTTCTCCGGG-3	5-ATGGTGTAGGATTGCGGAGC-3
Mouse GPX-1	5-CGTGCAATCAGTTCGGACAC-3	5-AAGGTAAAGAGCGGGTGAGC-3
Mouse GPX-3	5-ACCAATACCTTGAACTGAATGCAC-3	5-AATTAGGCACAAAGCCCCCA-3
Mouse GPX-6	5-TATGACCAAAGCCCACAGCA-3	5-TAACCGGCCAGTGCTTTGAA-3
Mouse GAPDH	5- CGTG CCGCCTGGAGAAAC-3	5-AGTGGGAGTTGCTG TTGAAGTC-3

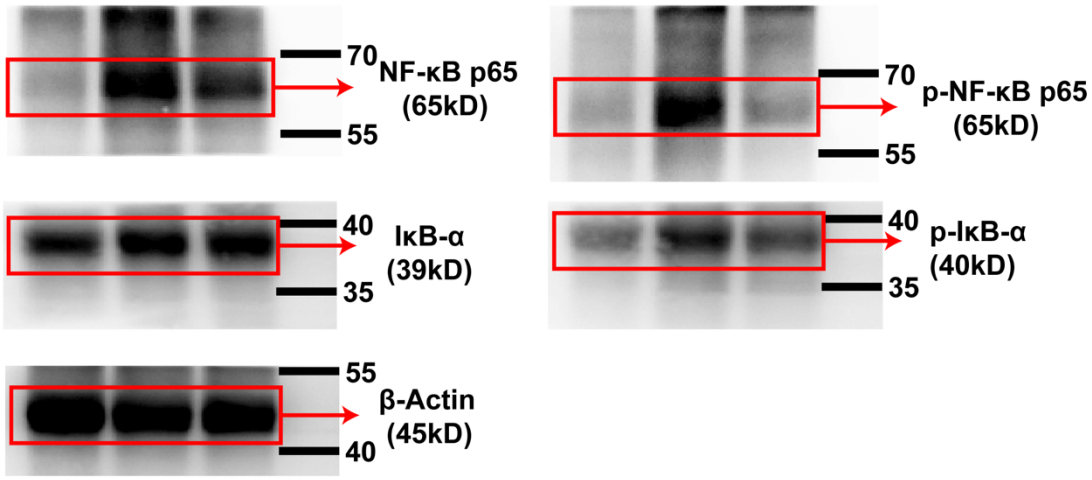

Supplementary Figure 31. Primary band images of western blot.

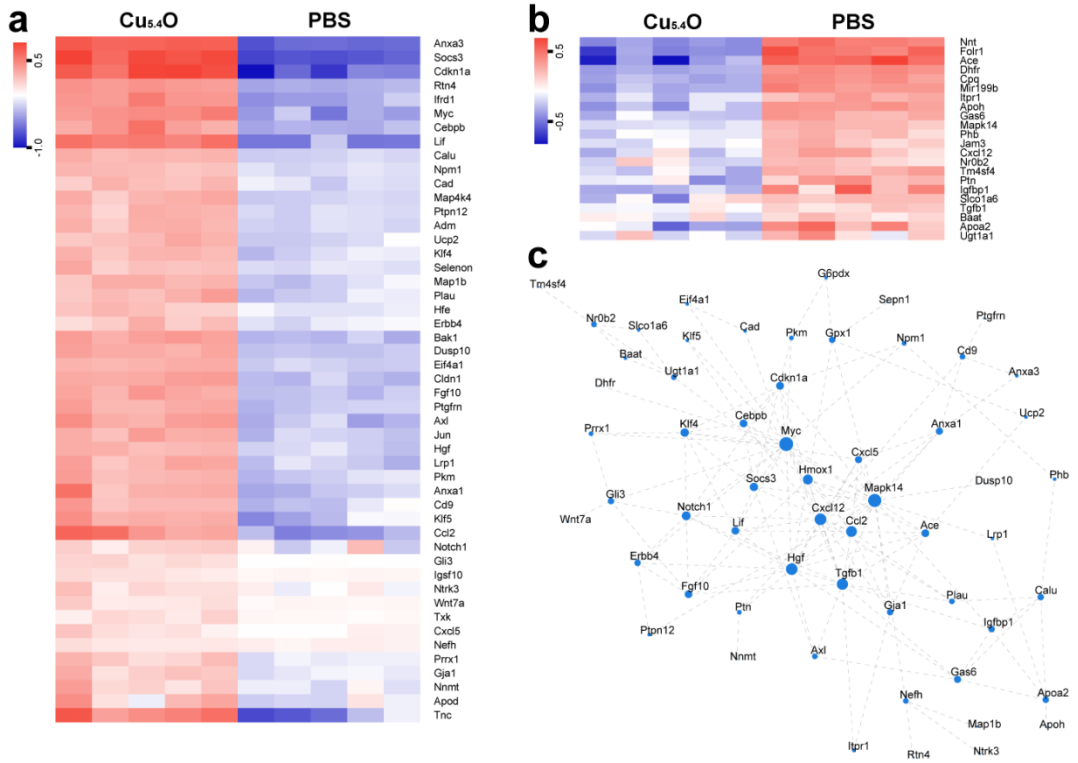

Supplementary Figure 32. Genes involved in tissue repair and regeneration. Heat maps of significantly (**a**) upregulated and (**b**) downregulated genes involved in tissue repair and regeneration after $Cu_{5.4}O$ USNPs treatment (fold change ≥ 2 and $p < 0.05$). (**c**) Protein-protein interaction network of differentially expressed genes involved in tissue repair and regeneration. Source data are provided as a Source Data file.

References

1. Qian, K. et al. Surface plasmon-driven water reduction: gold nanoparticle size matters. *J. Am. Chem. Soc.* **136,** 9842-9845 (2014).
2. Chen, S. J., Chien, F. C., Lin, G. Y. & Lee, K. C. Enhancement of the resolution of surface plasmon resonance biosensors by control of the size and distribution of nanoparticles. *Opt. Lett.* **29,** 1390-1392 (2014).
3. Giorgio, M., Trinei, M., Migliaccio, E. & Pelicci, P. G. Hydrogen peroxide: a metabolic by-product or a common mediator of ageing signals? *Nat. Rev. Mol. Cell Biol.* **8,** 722-728 (2007).

4. Sun, T. et al. A melanin-based natural antioxidant defense nanosystem for theranostic application in acute kidney injury. *Adv. Funct. Mater.* **29,** 1904833 (2019).
5. Jiang, D. et al. DNA origami nanostructures can exhibit preferential renal uptake and alleviate acute kidney injury. *Nat. Biomed. Eng.* **2,** 865-877 (2018).
6. Ni, D. L. et al. Molybdenum-based nanoclusters act as antioxidants and ameliorate acute kidney injury in mice. *Nat. Commun.* **9,** 5421 (2018).
7. Zhang, L. et al. Constructing metal-organic framework nanodots as bio-inspired artificial superoxide dismutase for alleviating endotoxemia. *Mater. Horiz.* **6,** 1682-1687 (2019).
8. Ni, D. et al. Ceria nanoparticles meet hepatic ischemia-reperfusion injury: the perfect imperfection. *Adv. Mater.* **31,** 1902956 (2019).
9. Li, L. et al. A broad-spectrum ROS-eliminating material for prevention of inflammation and drug-induced organ toxicity. *Adv. Sci.* **10,** 1800781 (2018).
10. Wu, H. et al. Ceria nanocrystals decorated mesoporous silica nanoparticle based ROS-scavenging tissue adhesive for highly efficient regenerative wound healing. *Biomaterials* **151,** 66-77 (2018).
11. Hao, C. L. et al. Chiral molecule-mediated porous Cu_xO nanoparticle clusters ameliorate Parkinson's disease by reducing oxidative stress. *J. Am. Chem. Soc.* **141,** 1091-1099 (2019).